Appendix A: Portfolios for Each Bridge Site

Bridge S041-63174

The bridge barriers on the north and the south bound of I-75 over 13 Mile Road (bridge S041-63174) were built in 2001. The bridge is oriented in the north-south direction, so the barriers have a west and east exposure. In general, the barriers are in good condition, no signs of map cracking, pop outs, delamination, or disintegration have been observed during the on-site investigation that was conducted by a survey team from WSU. The only form of distress that was observed was vertical cracking; on average the vertical cracks were spread 5 ft apart. Figure A-1 shows the locations on the barriers that were selected for coring by the survey team.

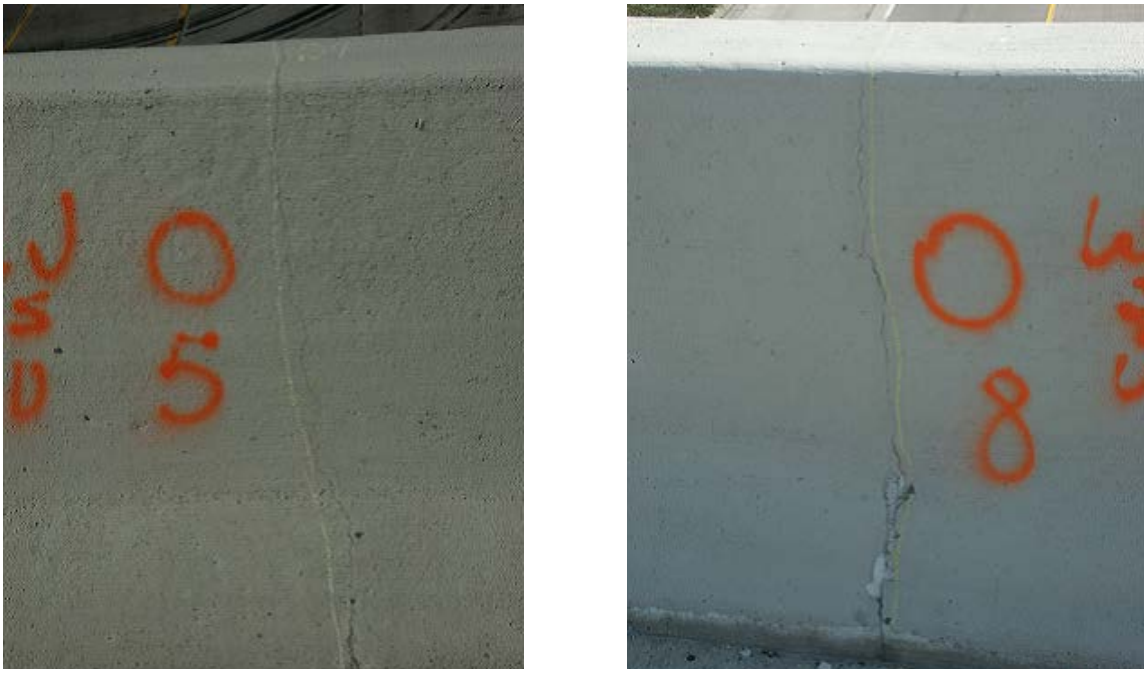

(a) Core A1- north bound, east exposure (b) Core A2 –south bound, east exposure

FigureA-1. Core specimen locations for S041-63174.

Visual Inspection of Core Specimens

Upon arrival at MTU, the cores from the barriers of the northbound and southbound were identified as A1 and A2 respectively. Photos of the 4-in diameter cores are shown in figure A-2. No steel reinforcement was present in the cores, however there was an imprint of existing rebar at the bottom of core A2 (figure A-3) with no sign of rust. The coarse aggregates were characterized as crushed tan carbonate rocks with a maximum size of 0.75 in. However, a visual inspection of polished slabs cut from the cores (figure A-4) revealed that some larger aggregates (up to 1 in) were present in A2 and also that the gradation of the aggregates in A2 was not as uniform as in A1.

Figure A-2. Cores evaluated for S041-63174, core A1 (left) and A2 (right).

Figure A-3. Imprint of rebar in core A2.

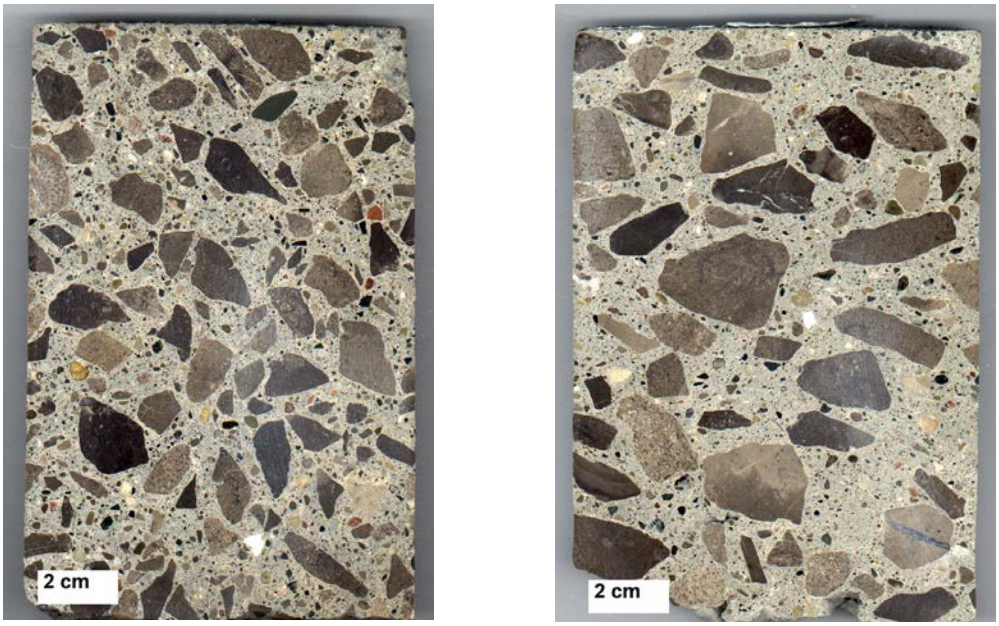

Figure A-4. Polished slabs from S041-63174, A1 (right) and A2 (left).

Stereo Optical Microscopy

The stereo optical microscope was used to examine polished slabs (figure A-4) cut from each core to assess general conditions of the concrete. Darker rims were visible on several siliceous fine aggregates (figure A-7); however, it was concluded that these were simply the result of weathering since no cracks or reaction products of ASR were apparent. As can be seen from figure A-5, a network of very small well-distributed unfilled air voids were present in each core. Also, some small entrapped air voids and cracked porous siltstones were observed here and there in the paste (figure A-6).

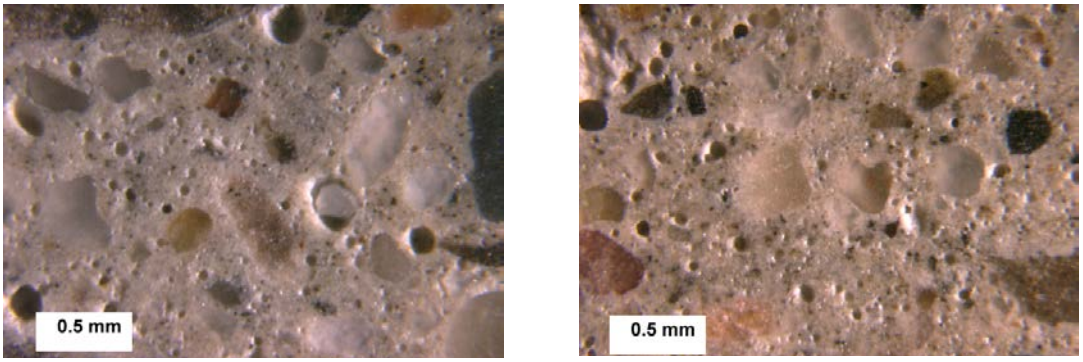

Figure A-5. Stereo optical micrograph showing the air void structure of A1 (right) and A2 (left).

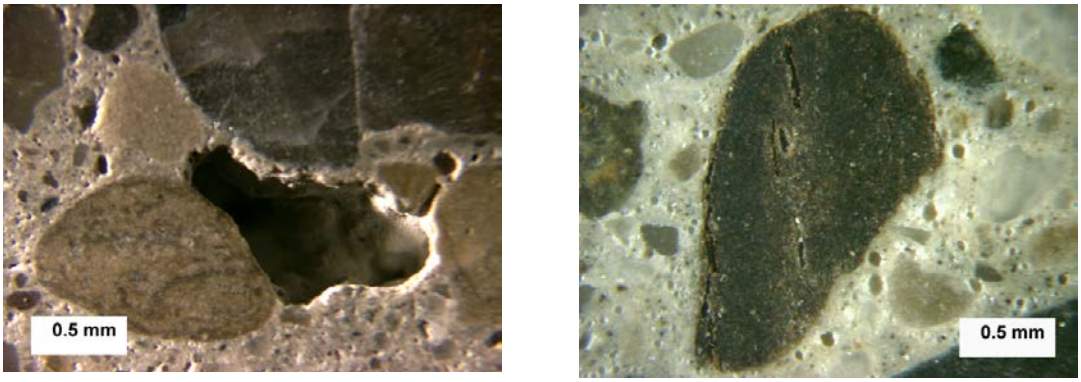

Figure A-6. Stereo optical micrograph of entrapped air void (left) and cracked fine siltstone (right) in core A1.

The stereo optical microscope was also used to determine the parameters of the air-void system in accordance to the modified point count method described in ASTM C 457. The results of the analysis are given in Table A-1.

Table A-1. Results from performing ASTM C457 on concrete from S041-63174.

ID MTU	Existing Specific surface (α) mm^{-1}	Existing Air Content (Area %)	Existing Spacing Factor (mm)	Paste (Area %)	Coarse Aggregate (Area %)	Fine Aggregate (Area %)	Extent of filled air voids
A1	40.1	5.6	0.112	26.4	37.4	30.5	None
A2	51.0	4.7	0.088	22.0	47.1	26.3	None

The recorded air contents are a little under the recommended minimum limit for 0.75 in top size aggregate (6 percent) because the air voids are very small; however, the spacing factor is well under 0.2 mm and the specific surface is well above 25 mm^{-1}. Consequently, the air-void system should provide adequate protection against freeze-thaw deterioration. The small size of the air voids might only become a problem in the future, as they get filled more easily with secondary deposits.

X-ray Analytical Microscopy

X-ray maps were recorded of the fine aggregates with darker rims. One of these maps is shown in figure A-7 together with a picture of the corresponding area on the slab. The map is presented as an RGB picture, where the red channel is used for the calcium, the green channel for the potassium and the blue channel for the silicon. The map shows that the fine aggregate is indeed a siliceous rock, but that the rim is simply due to weathering since neither micro-cracking, nor ASR reaction products (potassium), are present in the aggregate.

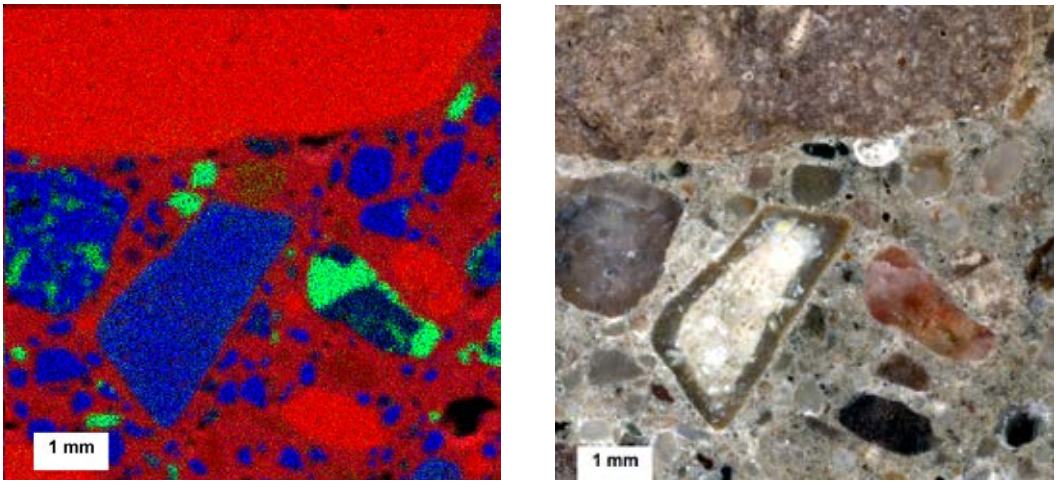

Figure A-7. X-ray map and picture of siliceous aggregate in core A1 (S041-63174). Red: Ca, green: K, blue: Si.

Petrographic Optical Microscopy

As can be seen from figure A-8, the analysis of a thin section made from concrete of S041-63174 indicates that the cracks present in the fine siltstones extend slightly through the paste. In some cases, the cracks were present only around the aggregate, as an aggregate-paste bond failure through the interfacial zone. Seen the high porosity of the siltstones, that feature might indicate the expulsion of water from the aggregate during freezing and thawing.

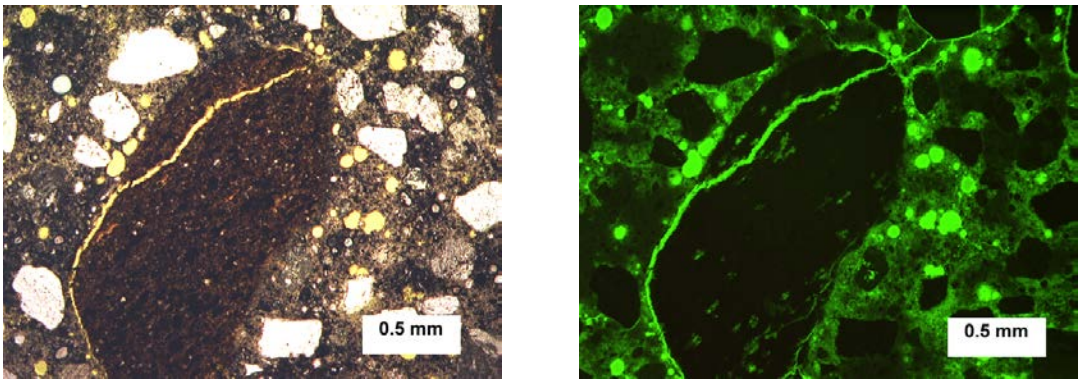

Figure A-8. Petrographic micrograph of typical cracked fine siltstone in concrete from S041-63174, plane polarized light and epifluorescent mode.

Scanning Electron Microscopy

The SEM was used in backscattered electron mode to record images of the cracked fine siltstones that were observed in thin-section. Also, a compositional x-ray map was recorded of such a siltstone in order to verify if any alkali-silica gel was present in the crack.

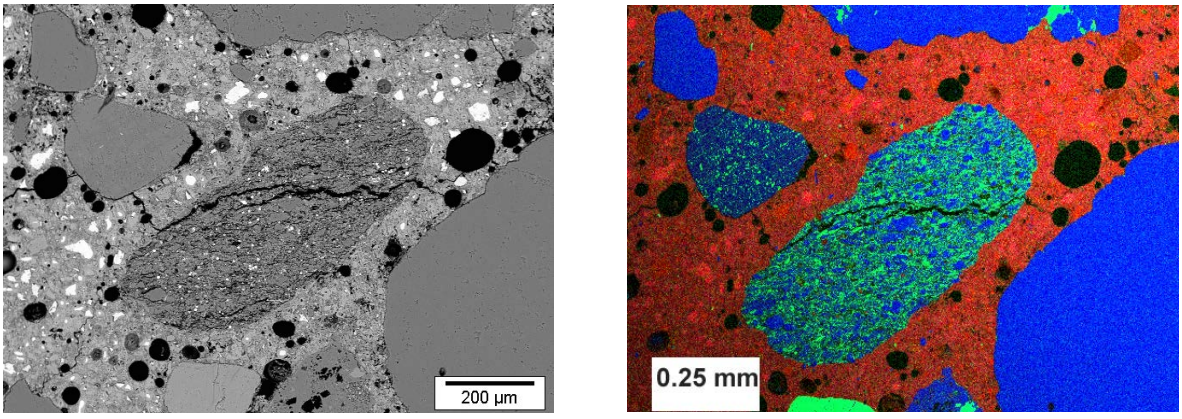

Figure A-9. SEM image (left) and x-ray map (right) of typical cracked siltstone in A1. Red: Ca, green: K, blue: Si.

Figure A-9, which represents an SEM image and a corresponding x-ray map (with the same color convention as the previous x-ray map) of a cracked siltstone, shows that no alkali-silica gel is present in, or in the vicinity of the aggregate. The cracks are thus more likely due to freeze-thaw deterioration rather than to ASR. Figure A-10 is an SEM image of an aggregate-paste bond failure through the interfacial zone of a siltstone. Figures A-9 and A-10 also show the high porosity of the fine siltstones.

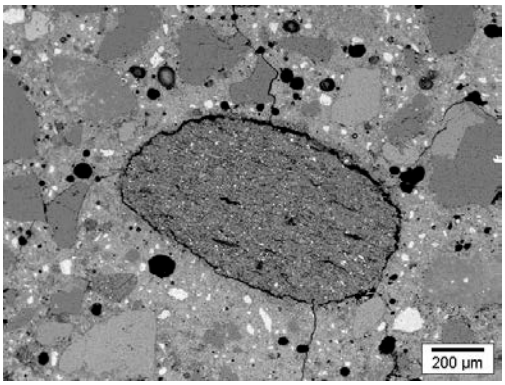

Figure A-10. SEM image of a typical siltstone in A1, aggregate-paste bond failure through the interfacial zone.

Depth of Carbonation

Polished billets from the top surface of the cores were tested for depth of carbonation using the phenolphthalein method. The recorded depths were between reasonable limits: 1 to 3mm for the first slab (A1) and 1 to 2 mm for the second (A2). This could mean that the outer layer of the concrete is relatively impermeable, or it could simply be due to the fact that the concrete was only one year old at the time of sampling.

Conclusion

Some vertical cracks, probably shrinkage cracks, are the only form of deterioration presently observed for the bridge barriers on I-75 over 13 Mile Road (bridge S041-63174). Remarkable features that were noticed during the petrographic evaluation are the presence of small entrapped air voids, relatively small entrained air voids (might be more susceptible to infilling by secondary deposits), a gap in the gradation of the aggregates in one of the cores, and the presence of porous fine siltstones. Those siltstones are often cracked; however, the cracks usually do not extend far into the paste. No proof of ASR was found to explain the cracks, although similar siltstones were reactive in samples from other sites. Considering the high porosity of those aggregates, the cracks might also be due to freeze-thaw damage. The time of appearance of ASR and freeze-thaw deterioration of aggregates is generally between 5 and 15 years, so the apparently good condition of the barrier is not a guarantee for future good performance.

Bridge S15-63172

The bridge barriers on the north and the south bound of I-75 over Clarkston Road (bridge S15-63172) were built in 1989. The bridge is oriented in the north-south direction, so the barriers have a west and east exposure. An on-site inspection of those barriers was performed by WSU. On average, map cracking and delamination were observed on 1% of the surface, and 9 vertical cracks, 2 horizontal cracks, and 5 pop outs were recorded per 36 ft horizontal segment. Figure A-11 shows the locations that were selected for coring by the survey team.

(a) Core B1-south bound, east exposure

(b) Core B2 –north bound, east exposure

Figure A-11. Core specimen locations for S15-63172.

Visual Inspection of Core Specimens

The cores from the south and the north bound were logged into MTU as B1 and B2, respectively. Photos of the obtained cores are shown in figure A-12. The coarse aggregate type was determined to be a mix of crushed and natural gravel with a maximum size of 0.75 in. Steel reinforcement was present at the bottom of core B1 (3.5 in from the surface) and embedded in core B2 (1.25 in from the surface), no rust was observed.

Figure A-12. Cores evaluated for S15-63172, B1 (left) and B2 (right).

Stereo Optical Microscopy

The stereo optical microscope was used to first examine polished slabs cut from each core to assess general conditions of the concrete (figure A-13). A photo of the air-void system of those slabs is shown in figure A-14. In general, the air voids are well distributed throughout the paste and only a few are filled; however, as can be seen from figure A-15, a significant amount of irregularly shaped voids are present around the aggregates and rebar.

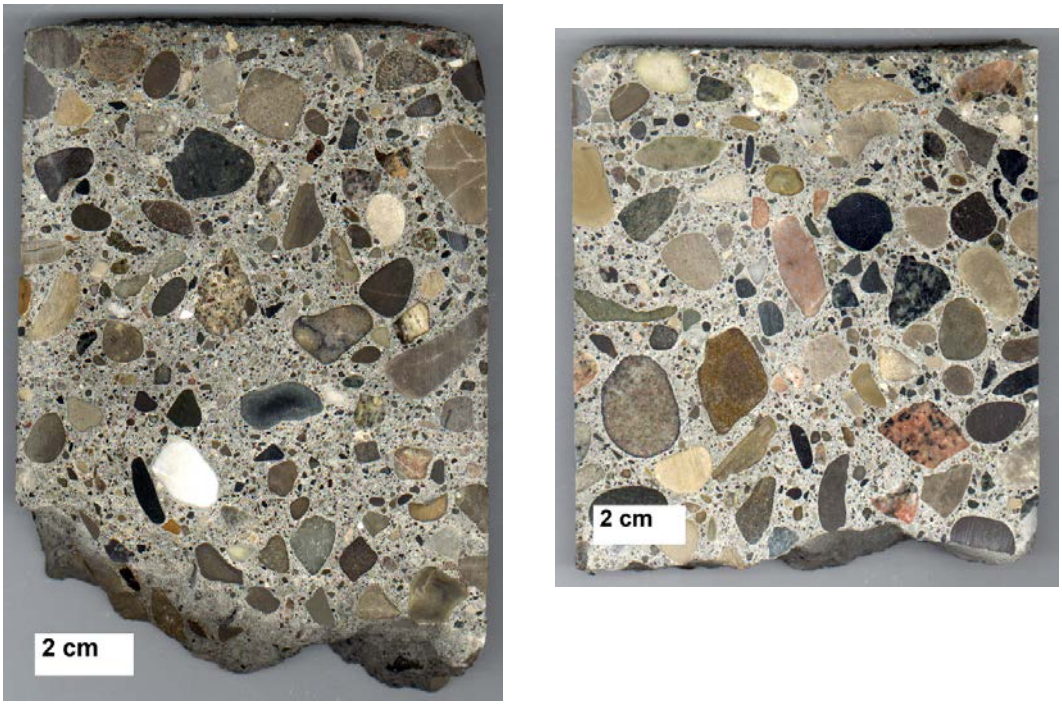

Figure A-13. Polished slabs from S15-63172, B1 (left) and B2 (right).

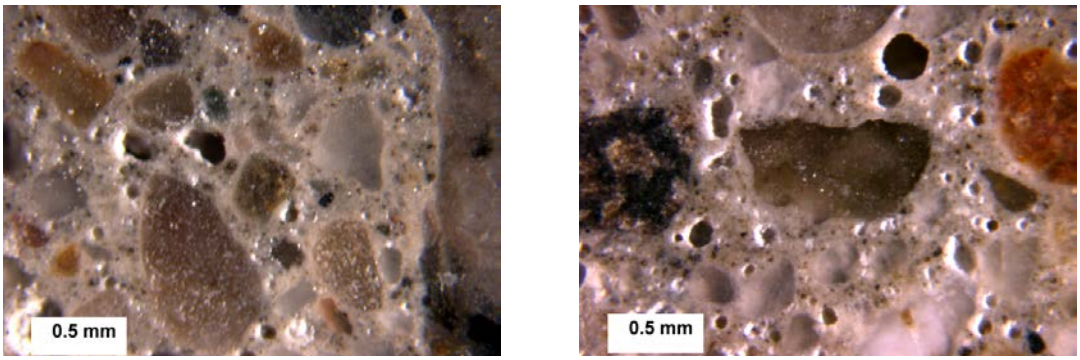

Figure A-14. Stereo optical micrograph showing air void structure of B1 (left) and B2 (right).

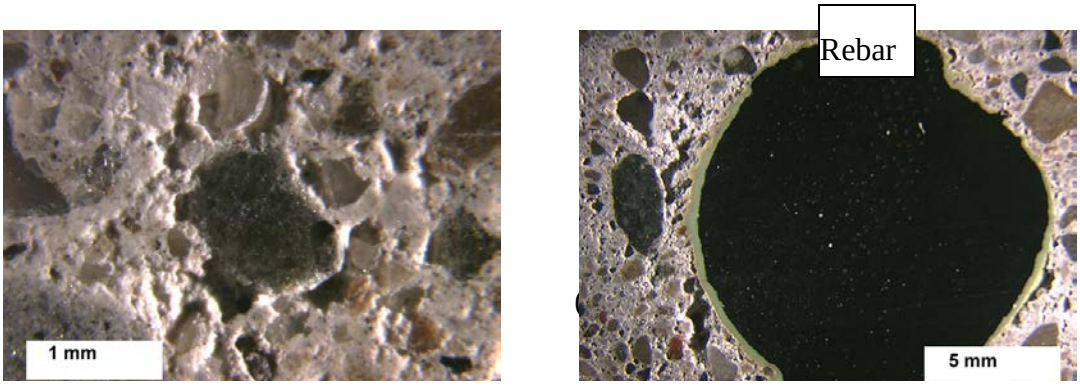

Figure A-15. Stereo optical micrograph of irregularly shaped voids around fine aggregates and rebar (S15-63172).

The stereo optical microscope was also used to determine the parameters of the air-void system in accordance to the modified point count method described in ASTM C 457. The results of the analysis are given in Table A-2.

Table A-2. Results from performing ASTM C457 on concrete from S15-63172.

ID MTU	Existing Specific surface (α) mm^{-1}	Existing Air Content (Area %)	Existing Spacing Factor (mm)	Paste (Area %)	Coarse Aggregate (Area %)	Fine Aggregate (Area %)	Extent of filled air voids
B1	36.1	4.2	0.123	19.0	39.1	37.6	Minor
B2	42.6	4.4	0.107	21.0	46.3	28.0	Minor

The recorded air contents are a little under the recommended minimum limit for 0.75 in top size aggregates (6 percent), maybe due to the relatively low paste content; however, the spacing factor is well under 0.2mm and the specific surface is well above 25 mm^{-1}. Consequently, the air-void system should provide an adequate protection against freeze-thaw deterioration.

Depth of Carbonation

Polished billets from the top surface of the cores were tested for depth of carbonation using the phenolphthalein method. The carbonation depth was found to be between 2 and 5 mm for both samples. These values are a little higher than normal and might indicate a concrete of lesser quality (more porous).

Conclusion

The bridge barriers on I-75 over Clarkston Road (bridge S15-63172), which were built in 1989, are in relatively good condition, with the exception of some vertical and horizontal cracks. The only remarkable features that were observed in the scope of this study are the presence of several relatively small entrapped air voids and a slightly high depth of carbonation, which might indicate a concrete of lesser quality.

Bridge S12-63172

The bridge barriers on the south and the north bound of I-75 over Clintonville (bridge S12-63172) were built in 1988. The bridge is oriented in the north-south direction, so the barriers have a west and east exposure. A survey team from WSU conducted an on-site investigation of those barriers. On average, map cracking was observed on only 1 percent of the surface; however, delamination covered 12 percent of the surface. Moreover, 14 vertical cracks, 1 horizontal crack and 18 popouts were recorded per 55 ft horizontal segment. Figure A-16 shows the locations that were selected for coring by the survey team.

(a) C1- south bound, east exposure (b) C2- north bound, west exposure

Figure A-16. Core specimen locations for S12-63172.

Visual Inspection of Core Specimens

The cores received from WSU were logged into MTU as C1 and C2 for the barriers exposed to the East (SB) and the West side (NB), respectively. Photos of the obtained cores are shown in figure A-17. The coarse aggregates were characterized as natural gravel with a maximum size of 0.75 in. Steel reinforcement was present in core C2 at 2.5 in from the top surface, no rust was observed.

Figure A-17. Cores evaluated for S12-63174 (10cm diameter), C1 (left) and C2 (right).

Stereo Optical Microscopy

The stereo optical microscope was used to first examine polished slabs cut from each core in order to assess the general condition of the concrete. The polished slabs are presented in figure A-18.

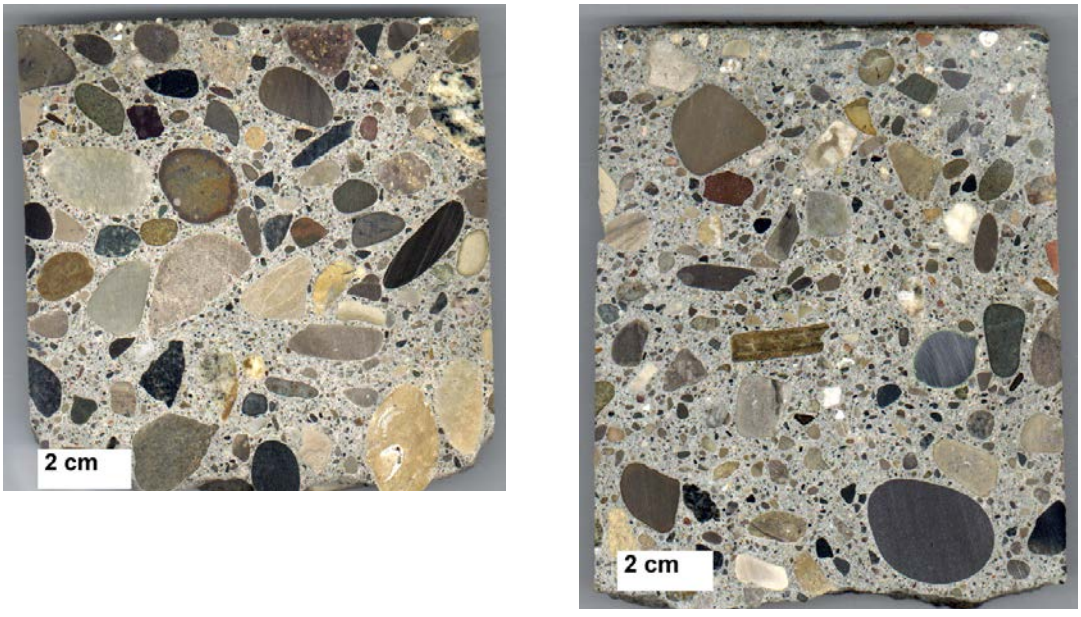

Figure A-18. Polished slabs from S12-63172, C1 (left) and C2 (right).

Entrapped air voids were present in slab C2 and in lesser extent in C1 (figure A-19). In both samples, the entrained air-voids were unevenly distributed, but only few were filled. Figure A-20 shows photos of locations where little air voids are present.

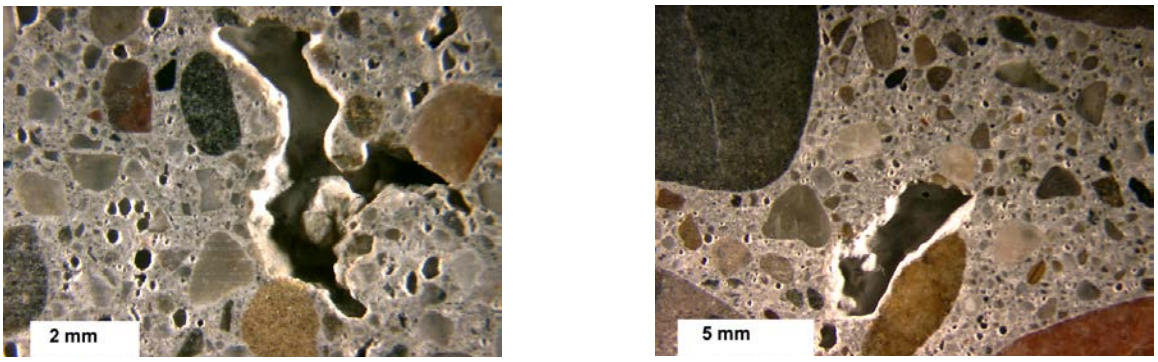

Figure A-19. Stereo optical micrograph of entrapped air in core C2.

The stereo optical microscope was also used to determine the parameters of the air-void system in accordance to the modified point count method described in ASTM C 457. The results of the analysis are given in Table A-3.

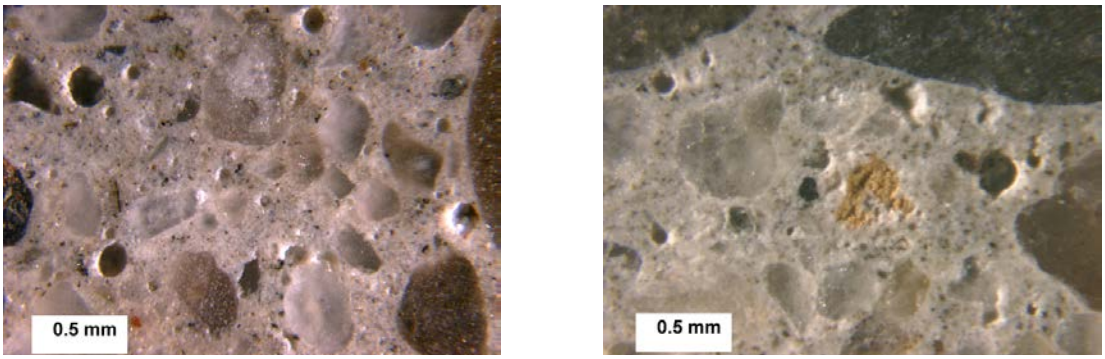

Figure A-20. Stereo optical micrograph of air void structures in C1 (right) and C2 (left).

Table A-3. Results from performing ASTM C457 on concrete from S12-63172.

ID MTU	Existing Specific surface (α) mm^{-1}	Existing Air Content (Area %)	Existing Spacing Factor (mm)	Paste (Area %)	Coarse Aggregate (Area %)	Fine Aggregate (Area %)	Extent of filled air voids
C1	35.9	6.5	0.072	16.9	50.6	25.9	Minor
C2	23.7	5.0	0.206	28.2	30.3	36.3	Minor

Sample C1 has an adequate spacing factor (< 0.2mm), specific surface (> $25mm^{-1}$) and air (> 6 percent) content, but the spacing factor for sample C2 was a little too high, and the specific surface and air content too low. Consequently, the air-void system of C2 might not be efficient in protecting the concrete against freeze-thaw deterioration.

Depth of Carbonation

Polished billets from the top surface of the cores were tested for depth of carbonation using the phenolphthalein method. The carbonation depth was between 2 and 4 mm below the barrier surface for C1 and between 1 and 3 mm for C2. This is only slightly higher than normal and might be due to the consolidation problem observed in the cores, or simply to the advanced age of the barriers.

Conclusion

The bridge barriers on I-75 near Clintonville (bridge S12-63172) were built in 1988. The major manifestation of distress on those barriers is delamination, which covers on average 12 percent of the surface. Also, some vertical and horizontal cracks as well as popouts are present. The possible causes of distress that were observed during this study are the lack of entrained air-voids (especially for the barriers from the southbound), and the presence of larger entrapped air voids.

Bridge S021-63174

The bridge barriers on the north bound of I-75 over Auburn road (bridge S12-63172) were built in 2001. A survey team from WSU performed an on-site investigation of the barriers with a west exposure. The barriers were found in a relatively good condition. Very little map cracking (0-2% of the surface) was observed, and no horizontal cracking, popouts, delamination, patch, and disintegration were recorded. On average, 5 vertical cracks, probably shrinkage cracks were observed per 8 ft segment. Figure A-21 shows one of the locations that were selected by the survey team for coring, no picture is available for the other location.

Figure A-21. Location of core D2 (S021-63174).

Visual Inspection of Core Specimens

The cores received from WSU were logged into MTU as D1 and D2. Photos of the obtained cores are shown in figure D-22. The coarse aggregates were characterized as crushed tan carbonate rocks with a maximum size of 0.75 mm. Steel reinforcement was present at the bottom of core D1 (11 cm from the surface), and an imprint of rebar was present at the bottom of D2 (12cm from the surface). No rust was observed; however, large gaps were present under and around the rebar in D1 (figure A-23). The imprint in D2 seems to indicate that the consolidation around the rebar was better at that location (figure A-23).

Figure A-22. Cores evaluated for S021-63174, D1 (left) and D2 (right).

Figure A-23. Steel reinforcement in cores D1 (left) and D2 (right). Poor consolidation around the rebar in D1.

Stereo Optical Microscopy

The stereo optical microscope was used to examine polished slabs cut from each core in order to assess the general condition of the concrete. The polished slabs are presented in figure A-24. The inspection revealed poor consolidation around some of the aggregates in D1 (figure A-25); however, the air-void system seemed to be adequate. A lot of entrained air-voids are well distributed in both samples (figure A-26).

The stereo optical microscope was also used to determine the parameters of the air-void system in accordance to the modified point count method described in ASTM C 457. The results of the analysis are given in table A-4. For both samples, the parameters of the air-void system are adequate (spacing factor < 0.2 mm, specific surface > 25 mm^{-1}, air

content > 6 percent). So, these barriers have an adequate protection against freeze-thaw deterioration.

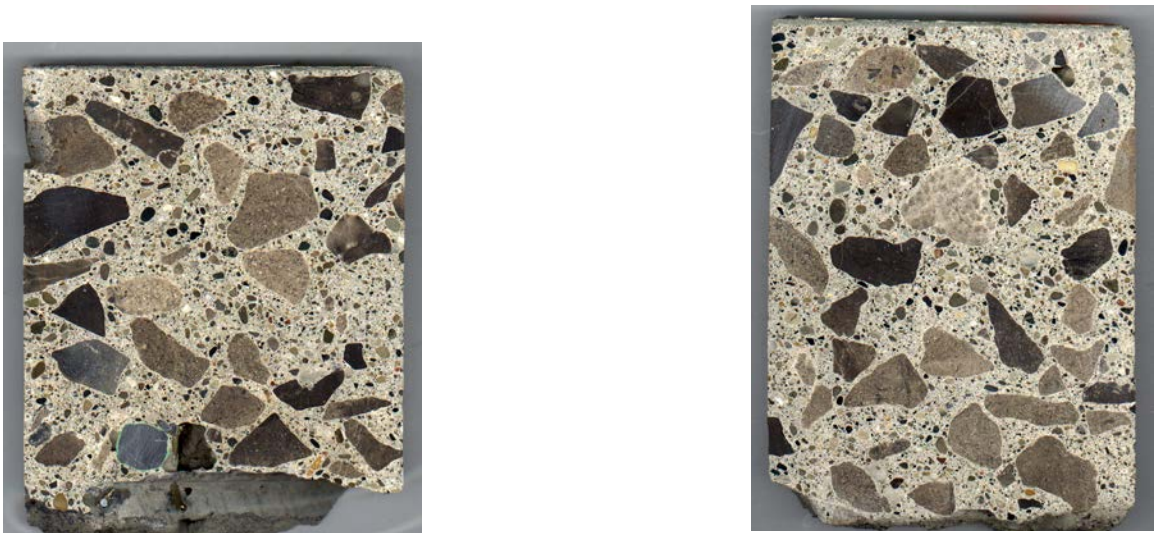

Figure A-24. Polished slabs from S021-63174, D1 (left) and D2 (right).

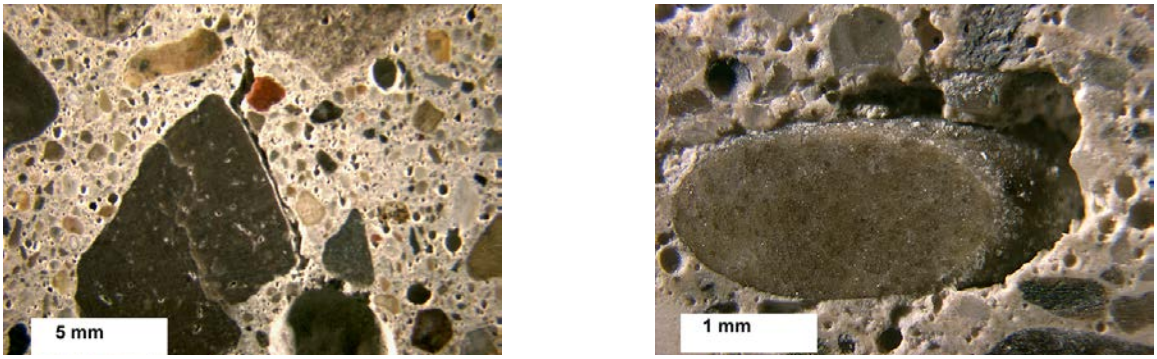

Figure A-25. Stereo optical micrograph of entrapped air around coarse and fine aggregates in D1.

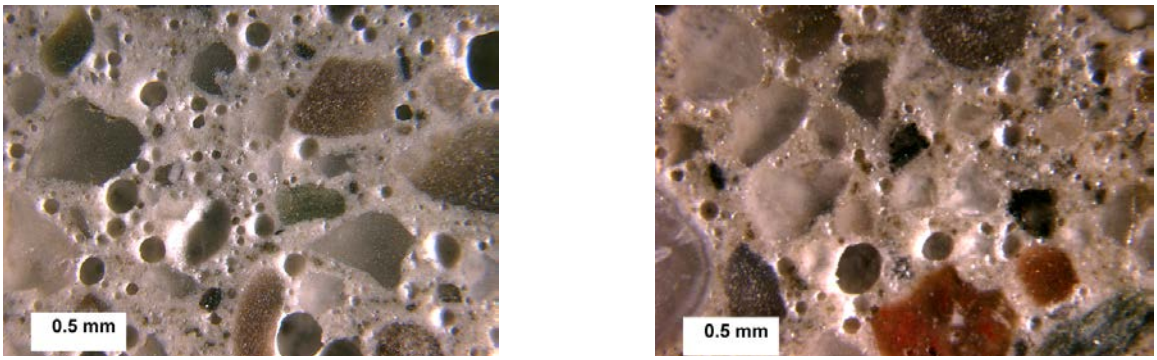

Figure A-26. Stereo optical micrograph of air void structure in D1 (left) and D2 (right).

Table A-4. Results from performing ASTM C457 on concrete from S021-63174.

ID MTU	Existing Specific surface (α) mm^{-1}	Existing Air Content (Area %)	Existing Spacing Factor (mm)	Paste (Area %)	Coarse Aggregate (Area %)	Fine Aggregate (Area %)	Extent of filled air voids
D1	36.2	7.3	0.072	19.1	40.1	33.6	None
D2	31.0	9.3	0.076	22.0	40.9	27.8	None

Depth of Carbonation

Polished billets from the top surface of the cores were tested for depth of carbonation using the phenolphthalein method. The carbonation depth was below 2 mm for both samples. This might indicate that the outer surface of the barriers is of good quality (not very porous), or this might be due to the fact that the barriers were only one year old at the time of sampling.

Conclusion

The bridge barriers on the north bound of I-75 over Auburn road (bridge S021-63174), were built in 2001, and are in a relatively good condition. The major manifestation of distress on those barriers is vertical cracking, probably due to shrinkage. The concrete has an adequate air-void system and no reactive aggregates were observed. The only possible cause of distress that was observed in this study is poor consolidation around the rebar and some of the aggregates.

Bridge S02-23152

The bridge barriers on the west bound of I96 above M43 (bridge S02-23152) were constructed in 1980. At that location the road is going in the North-South direction, so the barriers have a west and east exposure. A survey team from WSU performed an on-site investigation of those barriers. On average, 11 vertical cracks, no disintegration or spalling, 1 horizontal crack (no full length horizontal cracks), and one popout were observed per 40 ft horizontal segment. The locations of sampling selected by the survey team on the barriers with a west exposure are shown in figure A-27.

Figure A-27. Core specimen locations for S02-23152. E1 (left), E2 (right).

Visual Inspection

The cores were logged into MTU as E1 and E2 respectively. Photos of the obtained cores are shown in figure A-28. Note that the top of core E2 broke off right above the rebar (1.25 in from the surface) as a result of the corrosion and subsequent expansion of the corrosion product on the surface of the reinforcing steel. Rust was noted on rebar in both samples independently of the depth of embedment (up to 3 in from the surface for E1). Moreover, the paste did not adhere very well to the rebar. The coarse aggregates were characterized as natural gravel with a maximum size of 0.75 in.

Figure A-28. Cores evaluated for S02-23152, E1 (left) and top of E2 (right).

Figure A-29. Core E2 (bottom part), corrosion of reinforcing steel.

Stereo Optical Microscopy

The stereo optical microscope was used to examine polished slabs cut from each core (figure A-30) to assess general conditions of the concrete. The consolidation of the samples was adequate except around the rebar where the bond was not as good. The air-void system consisted of many well distributed air bubbles (figure A-31). Only very few air voids were filled.

Figure A-30. Polished slabs from S02-23152, E1 (left) and E2 (right).

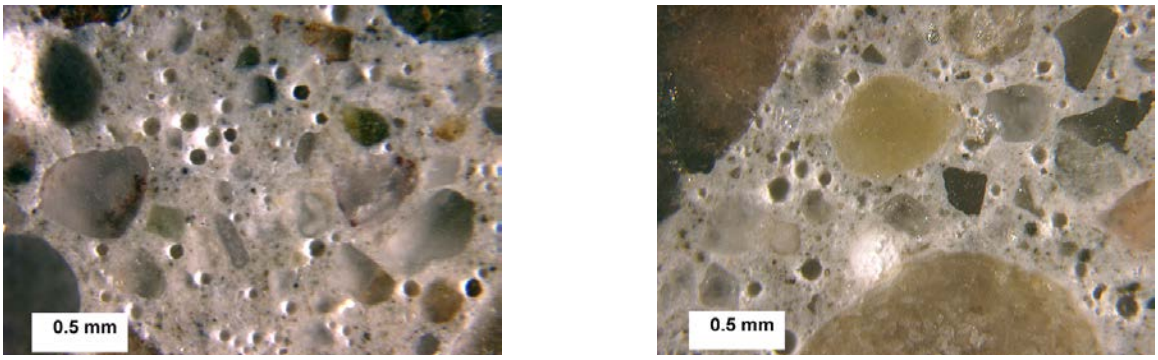

Figure A-31. Stereo micrograph showing air void structure of E1 (left) and E2 (right).

The stereo optical microscope was also used to determine the parameters of the air-void system in accordance to the modified point count method described in ASTM C 457. The results of the analysis are given in Table A-5.

Table A-5. Results from performing ASTM C457 on concrete from S02-23152.

ID MTU	Existing Specific surface (α) mm^{-1}	Existing Air Content (Area %)	Existing Spacing Factor (mm)	Paste (Area %)	Coarse Aggregate (Area %)	Fine Aggregate (Area %)	Extent of filled air voids
E1	28.8	7.0	0.120	24.3	42.5	26.2	Minor
E2	30.4	7.7	0.096	22.5	45.6	24.2	Minor

The recorded air content, spacing factor and specific surface are all satisfactory, so these barriers have an adequate air-void system to protect them against freezing and thawing.

Depth of Carbonation

Polished billets from the top surface of the cores were tested for depth of carbonation using the phenolphthalein method. The recorded depths were relatively high, from 4 to 10 mm for E1 and from 1.5 to 4 mm for E2. This indicates that the porosity of the outer layer of concrete is higher than normal. The concrete is thus more permeable to oxygen and deicing salts, which might contribute to the corrosion of the reinforcing steel.

Conclusion

The bridge barriers on the north and south bound of I96 over M43 (bridge S02-23152) were constructed in 1980. The major cause of distress observed in those barriers is the corrosion and subsequent expansion of the reinforcing steel leading to delamination of the outer layer of concrete. Also, the recorded depth of carbonation was higher than normal. This indicates that the outer layer of concrete is more permeable to aggressive

agents, which may be related to the corrosion of the reinforcing steel. A few filled air voids were observed, but too little to compromise the efficiency of the air-void system in protecting the concrete against freezing and thawing.

Bridge S04-82022

The bridge barriers on the east and west bound of I94 over Merriman (bridge S04-82022) were constructed in 1993. A survey team from WSU performed an on-site investigation of those barriers. On average, 28 percent of the surface was covered with map cracking, the most important form of deterioration observed. Seven vertical and one horizonal cracks, 8 popouts, and no delamination, patch or disintegration were observed per 18 ft segment. The locations on the barriers with a south exposure that were selected for coring by the survey team are shown in figure A-32.

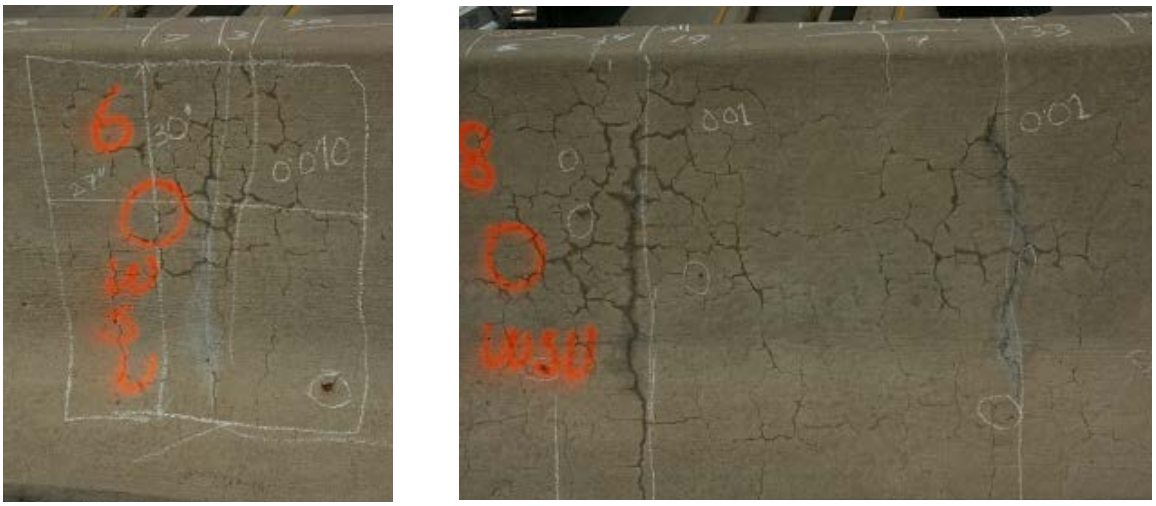

Figure A-32. Core specimen locations for S04-82022. Left is Westbound (F1) and right is Eastbound (F2)

Visual Inspection

The cores from the west and the east bound of I94, which are shown in figure A-32, were identified respectively as F1 and F2. Rebar was present in core F2 at approximately 3.5 in from the surface, but not in core F1, because F1 broke of at the location of the rebar (4 in from the surface) during the extraction. No rust was observed on the rebar of F2 or on the imprint in F1 (figure A-33). Cracks were observed at the top surface of both cores (figure A-34). The coarse aggregates were characterized as blast-furnace slag with a maximum size of 0.75 in.

Figure A-33. Cores evaluated for S04-82022, F1 (left) and F2 (right).

Figure A-34. Imprint of rebar in core F2.

Figure A-35. Map cracking at the top surface of cores F1 (left) and F2 (right).

Stereo Optical Microscopy

The stereo optical microscope was used to examine polished slabs cut from each core to assess general conditions of the concrete. As can be seen from the polished slabs in figure A-36, some entrapped air voids were present around one of the rebars in F2. Similar but smaller entrapped air-voids were also present here and there in the paste. The most striking feature of the concrete was the abundance of relatively porous cracked siltstones and fine chert aggregates with reaction rims and cracks extending through the paste, a typical sign of alkali-silica reactivity (ASR), (figure A-37).

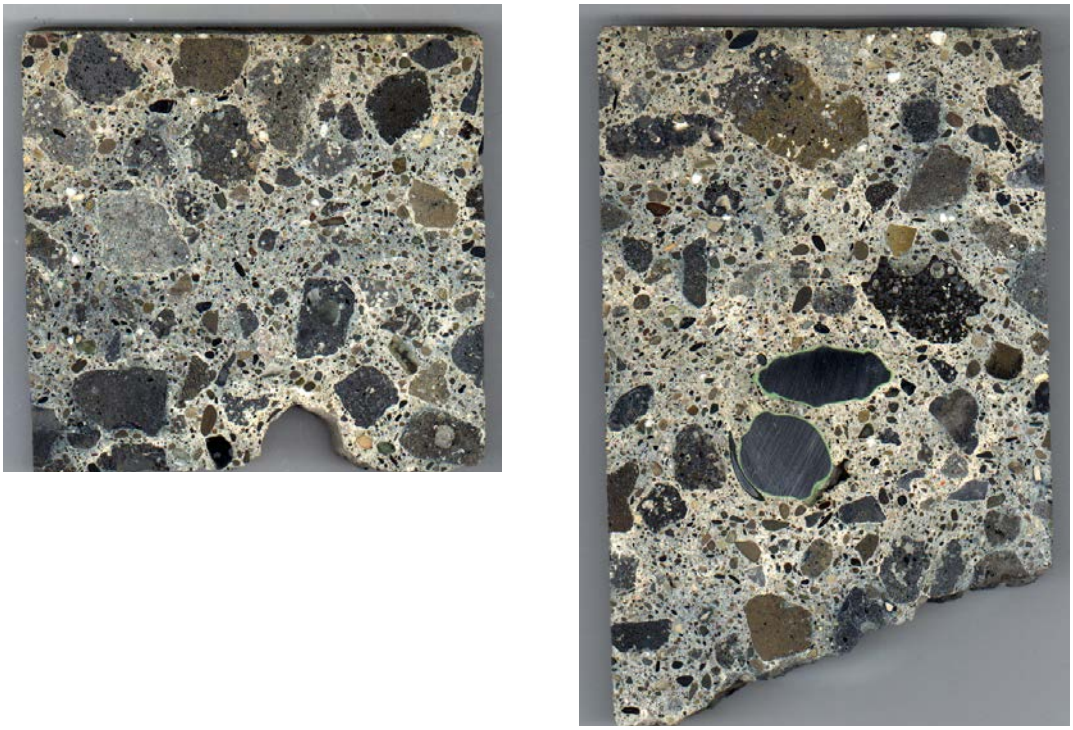

Figure A-36. Polished slabs from S04-82022, F1 (left) and F2 (right).

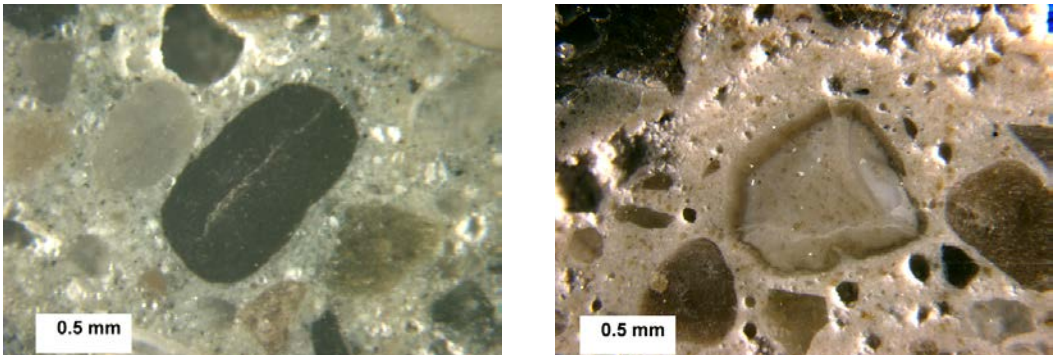

Figure A-37. Stereo optical micrographs of reacted fine chert and siltstone in F2.

A lot of well-distributed entrained air voids were present in the concrete; however, at some locations those were extensively filled with secondary deposits. Figure A-38 shows stereo optical micrographs of parts of the air-void system of slab F2 with and without serious infilling; the same phenomenon was observed in slab F1.

The stereo optical microscope was also used to determine the parameters of the air-void system in accordance to the modified point count method described in ASTM C 457. The results of the analysis are given in Table A-6.

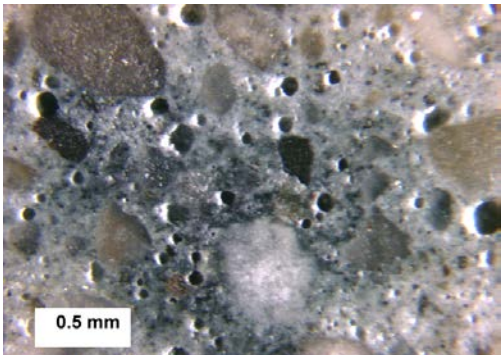

(a) No infilling

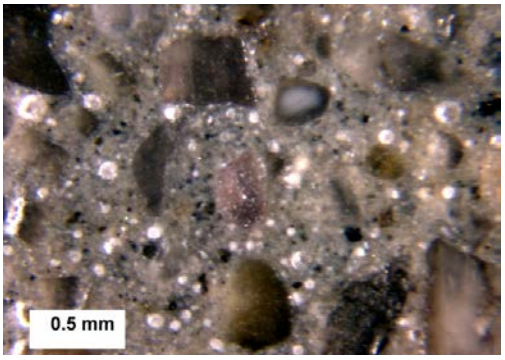

(b) Extensive infilling

Figure A-38. Stereo optical micrographs showing air void structure at different locations in slab F2.

Table A-6. Results from performing ASTM C457 on concrete from S04-82022.

ID MTU	Existing Specific surface (α) mm^{-1}	Existing Air Content (Area %)	Existing Spacing Factor (mm)	Paste (Area%)	Coarse Aggregate (Area %)	Fine Aggregate (Area %)	Extent of filled air voids
F1	15.4	8.8	0.203	27.4	30.6	32.7	Very Important
F2	25.4	6.6	0.173	29.2	45.6	18.4	Important

In both samples, the air content is above the recommended minimum limit (6 percent); however for sample F1 the spacing factor is at the maximum limit (0.2 mm) and the specific surface is under the recommended minimum (25 mm^{-1}). So, depending on the environmental conditions, F1 might suffer from freeze-thaw attack. Seeing the importance of the infilling, the original air-void system of these samples was probably adequate.

X-ray Analytical Microscopy

Some x-ray maps of aggregates showing signs of ASR were recorded with the x-ray analytical microscope. One of these maps is shown in figure A-39 together with a picture of the corresponding area on the slab. The map is presented as an RGB picture, where the red channel is used for the calcium, the green channel for the potassium and the blue channel for the silicon. Note the presence of potassium (alkali-silica gel) in the cracks. The maps confirm the reactivity of the fine chert aggregates but not of the cracked black siltstones (absent in figure A-39), because in that case the potassium is evenly distributed over the entire surface of the aggregate, so it is difficult to see from those maps if the potassium is there only as a natural constituent of the aggregate or also as a result of ASR.

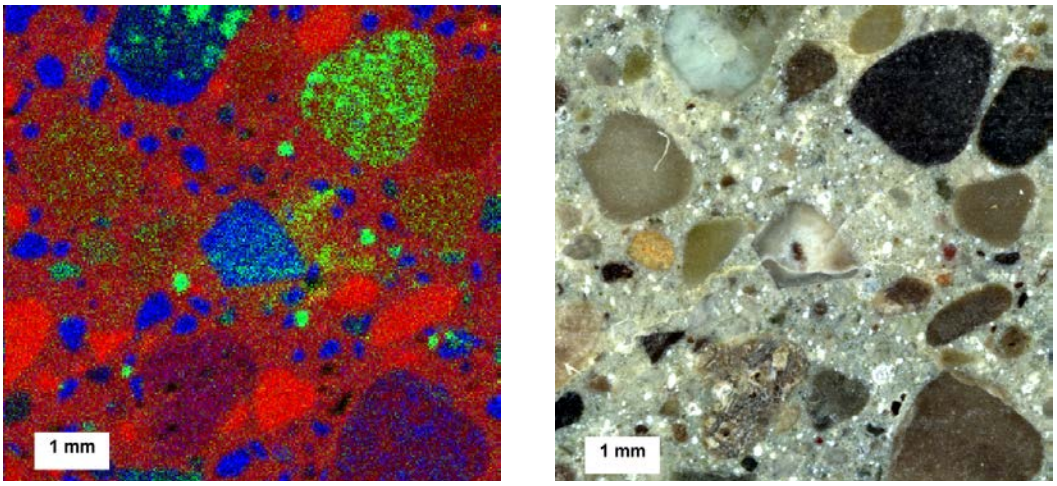

Figure A-39. X-ray map (left) and picture (right) of alkali silica reacted chert in F1. Red: Ca, green: K, blue: Si.

Petrographic Optical Microscopy

Thin sections viewed under the petrographic microscope confirmed the reactivity of the fine cherts, but also showed that the cracks initiating in the fine siltstones extend through the paste (figure A-40) and that in some cases those cracks are filled with some deposits, possibly alkali-silica gel. In addition, the deposits in the air-voids were recognized as needle-like ettringite crystals.

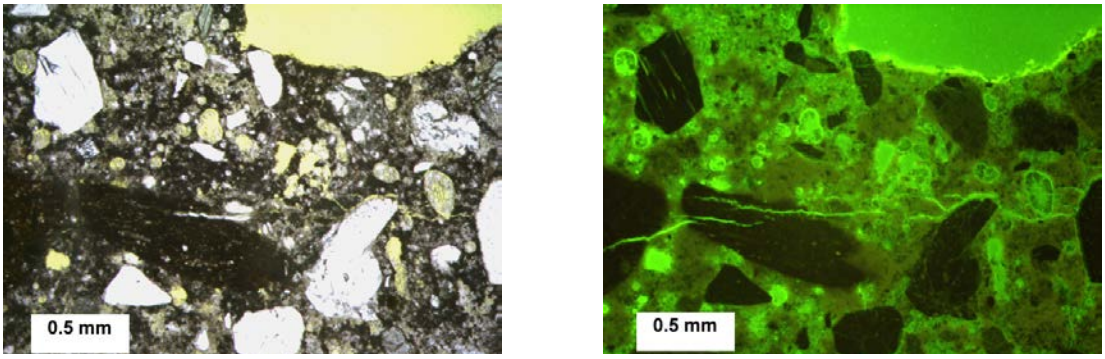

Petrographic micrograph of reactive fine siltstone and ettringite filled air voids in F1, plane polarized light (left) and epifluorescent mode (right).

Scanning Electron Microscopy

The SEM was used to make qualitative measurements of the composition of the infilling present in the air-voids and in the cracked siltstones and cherts. The results confirm the presence of ettringite (calcium sulfoaluminate gel) in the air voids, and the presence of

alkali-silica gel in the reacted aggregates and adjacent air voids. Figure A-41 shows a typical SEM micrograph (backscattered electron mode) and x-ray analysis of ettringite infilling air voids, note the needle-like crystals and how the biggest air-void is only partially filled. Figure A-42 shows an x-ray map (represented as an RGB picture with the same color convention as before) and SEM micrograph of an alkali-silica reactive siltstone. Alkali-silica gel (potassium-green) is present in the crack, but also in an air void adjacent to the aggregate (the locations are indicated on the SEM micrograph with black arrows). The concentration of potassium in alkali-silica gel is commonly lower further from the aggregate, which explains the lighter green color in the void.

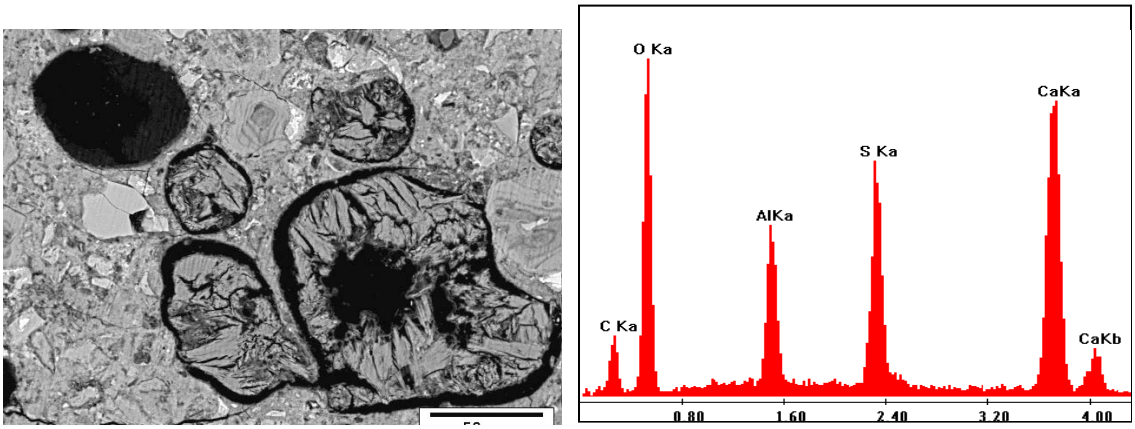

Figure A-40. SEM micrograph and x-ray spectrum (keV) for ettringite infilling air-voids in F1.

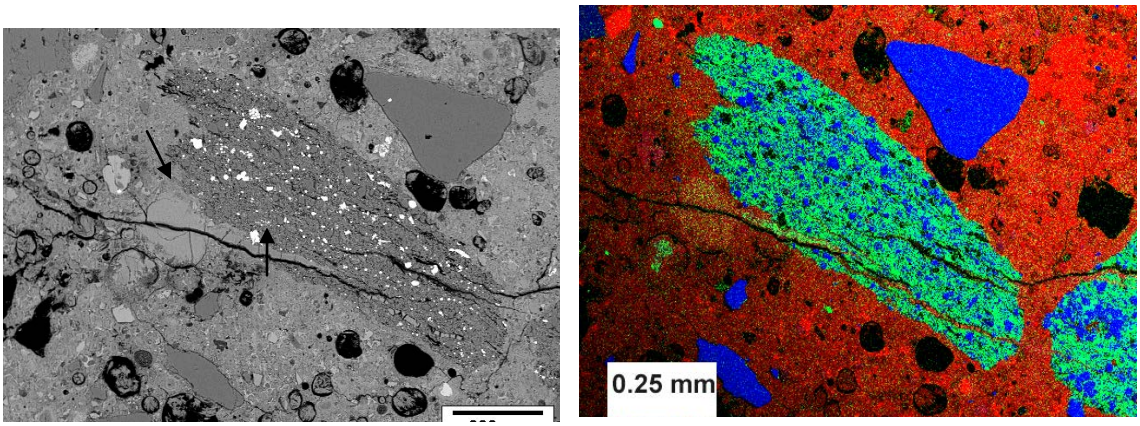

Figure A-41. SEM micrograph (left) and x-ray map of alkali-silica gel filling air void and crack.

As can be seen from figure A-42 the reactive siltstones are very porous, so these aggregates might also be frost-susceptible in addition to being reactive.

Conclusion

The primary cause of deterioration of the bridge barriers on I94 above Merriman (bridge S04-82022) is most probably alkali-silica reactivity. Indeed, several fine cherts and siltstones showing signs of ASR were observed in the cores. The fine siltstones might also be frost-susceptible, which would aggravate the deterioration by ASR. The results are consistent with the visual observations of distress reported from the field: on average 28 percent of the barriers are covered with map cracking, a common manifestation of ASR. The existing air-void spacing factor was also found to be marginal; however, this is mainly due to the extensive secondary ettringite infilling. The presence of ettringite is most likely a consequence of the increased permeability resulting from the deterioration by ASR, since no damaging effect of sulfate attack was observed. Finally, some small consolidation problems were observed in the concrete.

Bridge S01-44044

The bridge barriers on the west bound of I96 over Clark road (bridge S01-44044) were built in 1983. A team from WSU performed an on-site inspection of those barriers. On average, map cracking was observed on 3 percent of the surface, and 4 vertical cracks and 1 horizontal cracks were recorded per 12 ft of barrier. No popouts, delamination, patch or disintegration were observed. The team from WSU selected two locations of sampling on the barriers with a south exposure (figure A-43).

Figure A-43. Core specimen locations for S01-44044, G1 (left) and G2 (right).

Visual Inspection of Core Specimens

Photos of the obtained cores are shown in figure A-44. As can be seen, the concrete is not well consolidated; the honeycombing in core G2 was even so important that it broke diametrically in two pieces. The coarse aggregates consisted of tan carbonate rocks with a maximum size of 0.75 in. No steel reinforcement was present in the cores.

Figure A-44. Cores evaluated for S01-44044, G1 (left) and G2 (right).

Stereo Optical Microscopy

After gluing core G2 back together with epoxy, polished slabs from each core (figure A-45) were observed with the stereo optical microscope to assess general conditions of the concrete. As can be seen from figure A-46, not many air-voids are present in the concrete, and most of them are filled with ettringite. Some fine siliceous aggregates with darker rims were observed; however, very few of those were cracked and when they were, the cracks never extended through the paste.

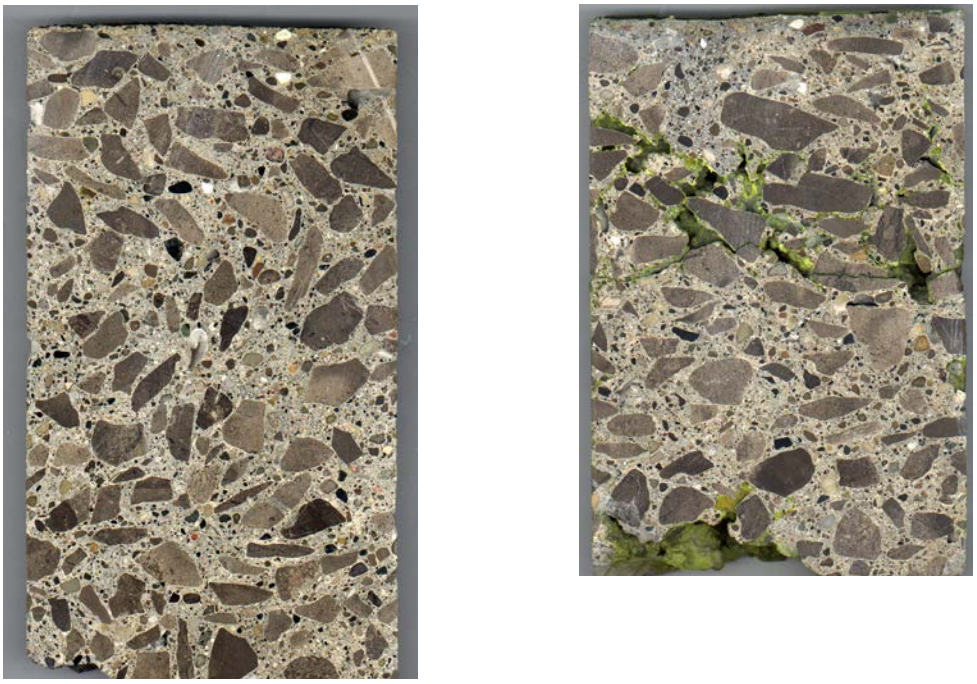

Figure A-45. Polished slabs from S01-44044, G1 (left) and G2 (right).

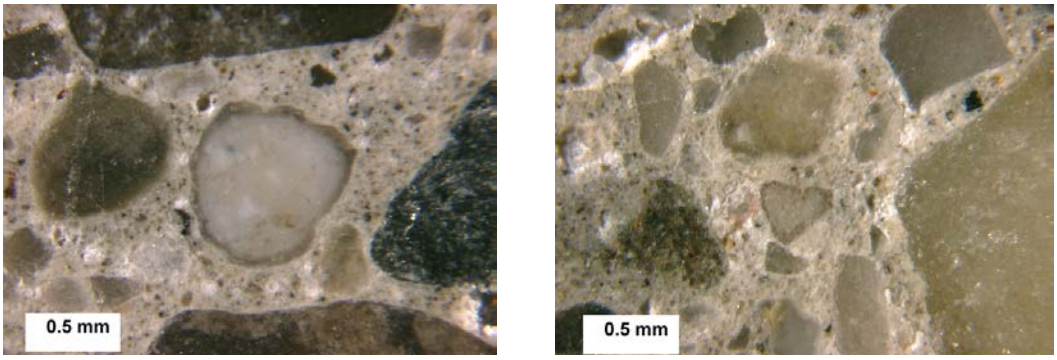

Figure A-46. Stereo optical micrograph showing air void structure of G1 (left) and G2 (right).

The stereo optical microscope was also used to determine the parameters of the air-void system in accordance to the modified point count method described in ASTM C 457. The results of the analysis are given in table A-7.

Table A-7. Results from performing ASTM C457 on concrete from S01-44044.

ID MTU	Existing Specific surface (α) mm^{-1}	Existing Air Content (Area %)	Existing Spacing Factor (mm)	Paste (Area %)	Coarse Aggregate (Area %)	Fine Aggregate (Area %)	Extent of filled air voids
G1	9.9	6.0	0.434	25.1	29.8	38.0	Very Important
G2	3.7	7.8	0.784	22.0	39.9	29.2	Very important

The existing air contents are acceptable, but they result from a large amount of entrapped air rather than from a large amount of entrained air. Also, since little unfilled air voids are present in the paste, the existing spacing factor is significantly higher than the 0.2 mm limit and the specific surface is greatly under the 25 mm^{-1} minimum recommended value. Therefore, the concrete is not adequately protected against freeze-thaw deterioration.

Although the staining method that was supposed to selectively stain the ettringite filled voids purple did not provide the desired results, coloring both, the paste and the filled voids light pink, an attempt was made to record the number of filled air voids as well as the number of empty voids (ASTM C457, requires only the computation of the existing air voids, since only they can actually protect the paste against frost damage). The original spacing factors (calculated including the filled and empty air voids) were estimated at 0.21 mm and 0.308 mm for G1 and G2 respectively, which are less than half of the existing spacing factors, but still in excess of the 0.2 mm limit. Consequently, even before the infilling the amount of entrained air voids might not have been satisfactory.

X-ray Analytical Microscopy

An x-ray analytical microscope was used to record X-ray maps of the fine aggregates showing darker rims. One of these maps is shown in figure A-47 together with a picture of the corresponding area on the slab. The map is presented as an RGB picture, where the red channel is used for the calcium, the green channel for the potassium and the blue channel for the silicon. As can be seen, no potassium is present in the siliceous fine aggregate and the crack does not extend through the paste; therefore, the reaction rim and the crack are probably simply due to weathering and not to ASR.

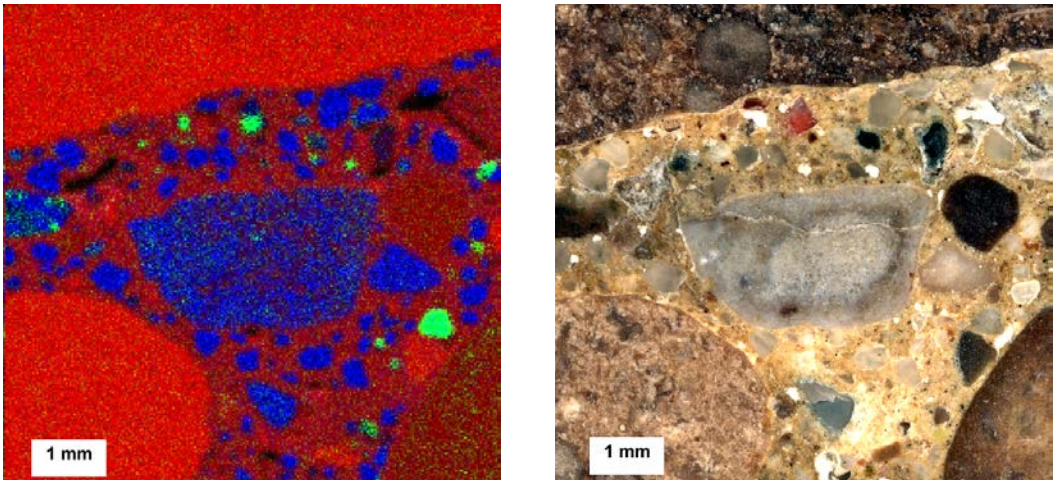

Figure A-47. X-ray map and picture of fine aggregate in G2. Red: Ca, green: K, blue: Si.

Petrographic Optical Microscopy

The petrographic micrographs presented in figure A-48 show typical needle-like crystals of ettringite infilling air-voids in G2.

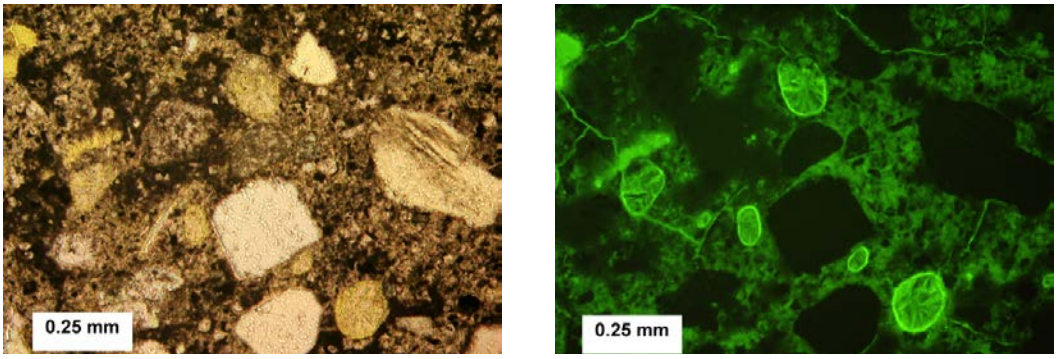

Figure A-48. Petrographic micrographs of ettringite infilling entrained air voids in G2, plane polarized light (left) and epifluorescent mode (right).

Scanning Electron Microscopy

The SEM-EDS was used to confirm the presence of ettringite (calcium sulfoaluminate) in air voids. Figure A-49 presents an SEM image of ettringite (calcium sulfoaluminate) filled voids with a corresponding x-ray map recorded from specimen G2. The map is present as an RGB picture, where the red channel is used for the aluminum, the green channel for the calcium and the blue channel for the sulfur. The filled voids have a purple color on the map, which indicates that both aluminum (red) and sulfur (bluu) are present, two major constituents of ettringite.

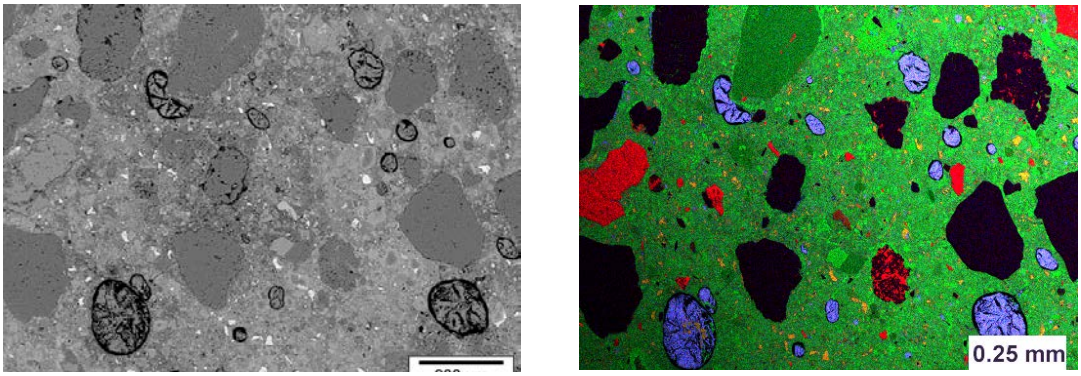

Figure A-49. SEM image and x-ray map of ettringite filled voids in G2.

Depth of Carbonation

Polished billets from the top surface of the cores were tested for depth of carbonation using the phenolphthalein method. The recorded depth of carbonation was between 1.5 and 3 mm for G1 and between 2 and 4 mm for G2. These values are only a little higher than normal, and might be due to the increase in permeability resulting from poor consolidation.

Conclusion

The concrete from the bridge barriers on I96 over Clark road (bridge S01-44044) is of very poor quality. Indeed, the cores contained a lot of large entrapped air voids (honeycombing), and the parameters of the existing air-void system were unsatisfactory to protect the paste against freeze-thaw attack. Most of the air voids were filled with secondary ettringite, and the initial air-void system (before infilling) might or might not have been adequate. Also, it is very probable that dissolution and precipitation of secondary ettringite was favored by poor consolidation.

Bridge S06-82022

The bridge barriers on the west bound of I94 over Middlebelt (bridge S06-82022) were constructed in 1993. A survey team from WSU performed an on-site inspection of those barriers. They were found in a very poor condition; on average, map cracking covered 65 percent of the surface, and 16 vertical and 2 horizontal cracks were present per 18 ft of barrier length. Pop outs, delamination, patch, spall and disintegration were not a problem. The locations of sampling on the barriers with a south exposure, as selected by the team from WSU, are shown in figure A-50.

Figure A-50. Core specimen locations for S06-82022, H1 (left) and H2 (right).

Visual Inspection of Core Specimens

Photos of the cores identified as H1 and H2 are shown in figure A-51. The coarse aggregates were composed of blast furnace slag with a maximum size of 0.75 in. A little rust was observed on the sides of the rebar in core H1. An imprint of rebar was present on the side of core H2, however no sign of rust was noticed. Some entrapped air voids were visible on the sides of the cores, and on the rebar imprint.

Figure A-51. Cores evaluated for S06-82022, H1 (left) and H2 (right).

Stereo Optical Microscope Tests

The stereo optical microscope was used to examine polished slabs cut from each core (figure A-52) to assess general conditions of the concrete. A network of well-distributed entrained air voids was present in each core; however, at some locations most of those where filled with secondary deposits (figure A-53), or larger irregularly shaped air voids were present (figure A-54). Some fine siliceous aggregates with darker rims and cracks sometimes extending through the paste were observed (figure A-54), indicating the possibility of ASR. Also, several fine black siltstones with lengthwise cracks were present.

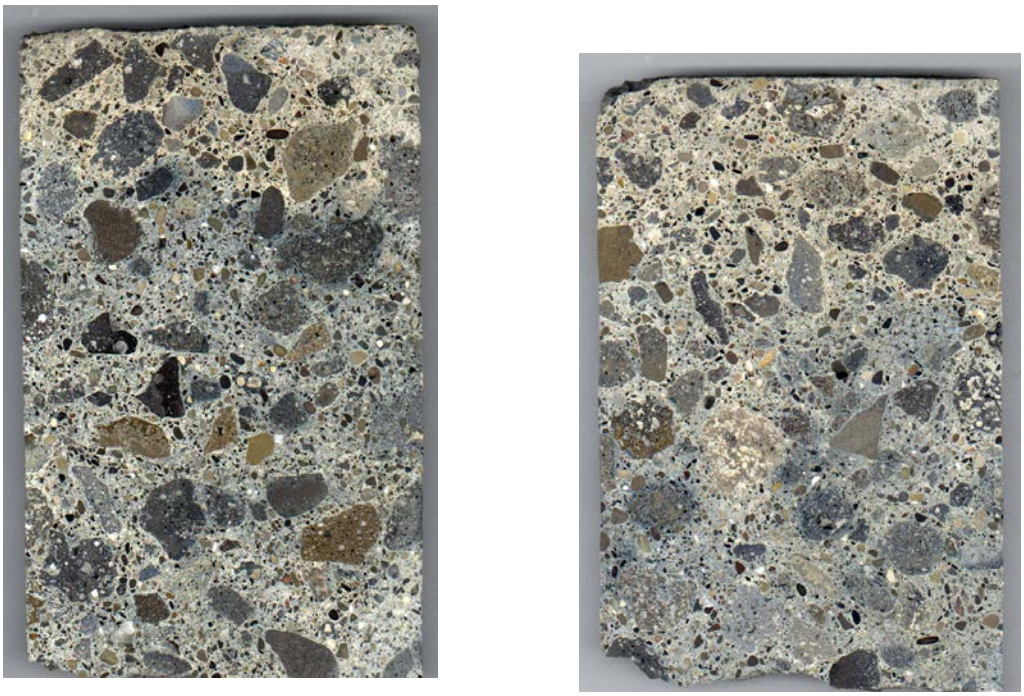

Figure A-52. Polished slabs from S06-82022, H1 (left) and H2 (right).

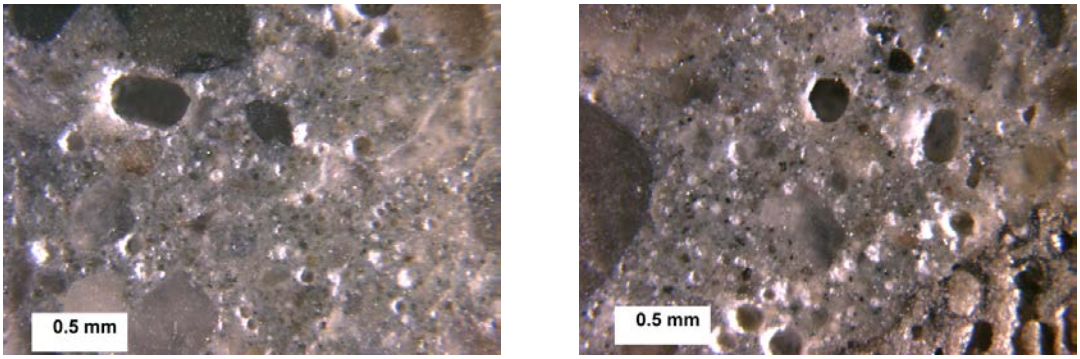

Figure A-53. Stereo optical micrograph showing air-void structure of H1 (left) and H2 (right).

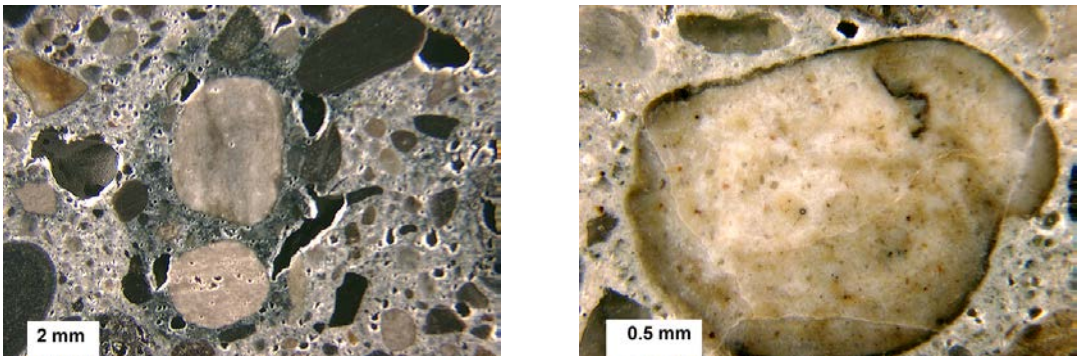

Figure A-54. Stereo optical micrograph of entrapped air and cracked aggregate in H2 (left) and H1 (right).

The stereo optical microscope was also used to determine the parameters of the air-void system in accordance to the modified point count method described in ASTM C 457. The results of the analysis are given in table A-8.

Table A-8. Results from performing ASTM C457 on concrete from S06-82022.

ID MTU	Existing Specific surface (α) mm^{-1}	Existing Air Content (Area %)	Existing Spacing Factor (mm)	Paste (Area %)	Coarse Aggregate (Area %)	Fine Aggregate (Area %)	Extent of filled air voids
H1	19.1	12.6	0.180	26.1	27.9	33.4	Important
H2	7.6	12.8	0.304	29.0	28.7	28.6	Very important

The recorded air contents are well above the minimum recommended limit, partly because of the presence of entrapped air-voids and the high porosity of the slag aggregates; however, the spacing factor for H2 is too high, since the infilling of the air-voids is so important. Also, the specific surface is too low for both samples, which indicates that the mean size of the unfilled air voids is rather large. Indeed, as can be seen in figure A-53, most of the smaller air voids are filled with secondary deposits. In observing the large amount of infilled air voids, it is very probable that the spacing factor was adequate before the infilling, and that the original air content was grossly higher than the specified value.

X-ray Analytical Microscopy

X-ray maps were recorded of the fine siliceous aggregates showing darker rims and of the cracked siltstones. One of these maps is shown in figure A-55 together with a picture of the corresponding area on the slab. The map is presented as an RGB picture, where the red channel is used for the calcium, the green channel for the potassium and the blue channel for the silicon. The maps confirm that the fine siliceous aggregates are undergoing ASR; indeed they show the presence of alkali-silica gel (potassium) in the cracks. On the other hand, potassium is present everywhere in the black siltstones (in the bottom left corner of figure A-55), so it not obvious from those maps if the potassium is there as a result of ASR or naturally occurring in that type of aggregate.

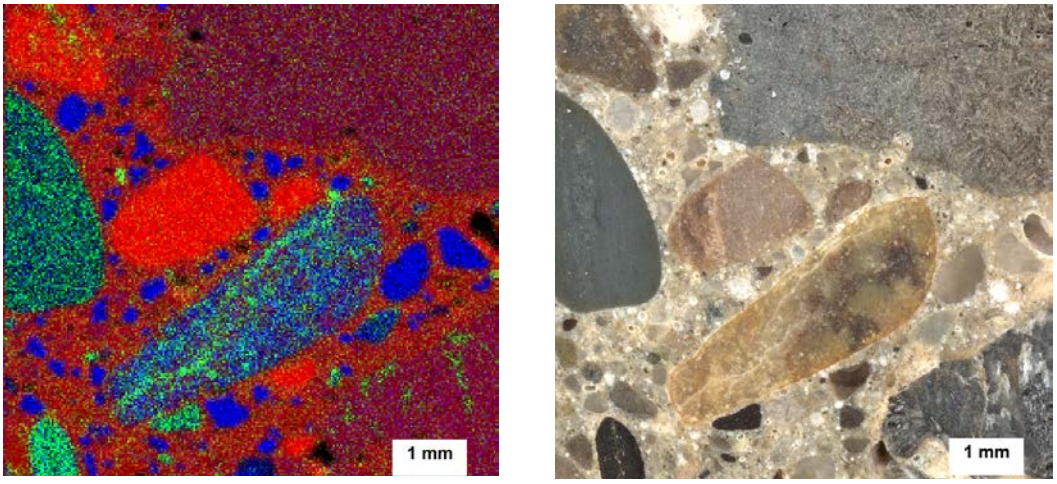

Figure A-55. X-ray map (left) and picture of reacted aggregate (right) in H1. Red: Ca, green: K, blue: Si.

Petrographic Optical Microscopy

The petrographic microscope confirmed the alkali-silica reactivity of the cherts, but also showed that the cracks present in the siltstones were extending through the paste. Although alkali-silica gel was not extensively observed in the siltstones, the crack pattern and the fact that the same stones were found reactive in other samples indicate that they are probably also alkali-silica reactive. Seen the high porosity of the siltstones, freeze-

thaw damage might also play a role in the deterioration. Figure A-56 shows petrographic micrographs of a reacted siltstone with cracks extending through the paste, and figure A-57 shows a reactive chert.

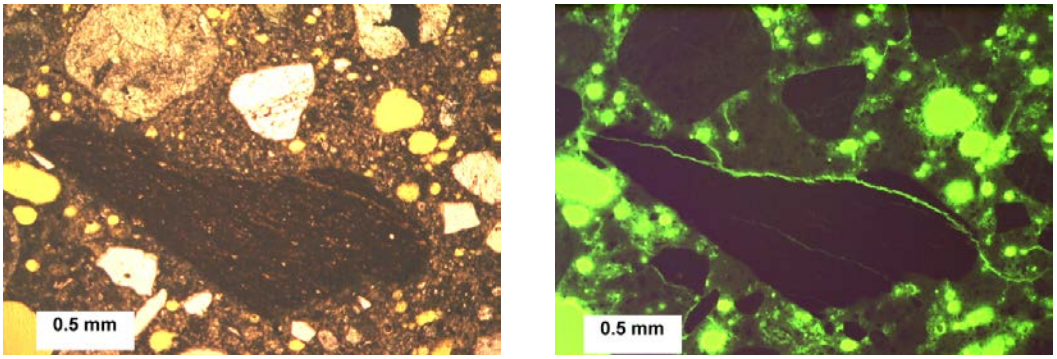

Figure A-56. Petrographic micrograph of reactive siltstone in H1, transmitted plane polarized light (left) and epifluorescent mode (right).

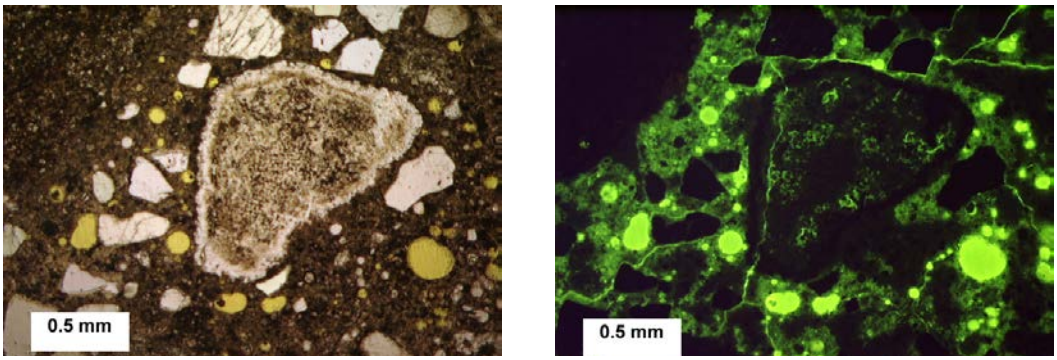

Figure A-57. Petrographic micrograph of reactive siltstone in H1, plane polarized light (left) and epifluorescent mode (right).

Scanning Electron Microscopy

The SEM was used to confirm the reactivity of the cherts and siltstones. Figures A-58 shows SEM images of reacted cherts and siltstones. The high porosity of the siltstones is clearly visible.

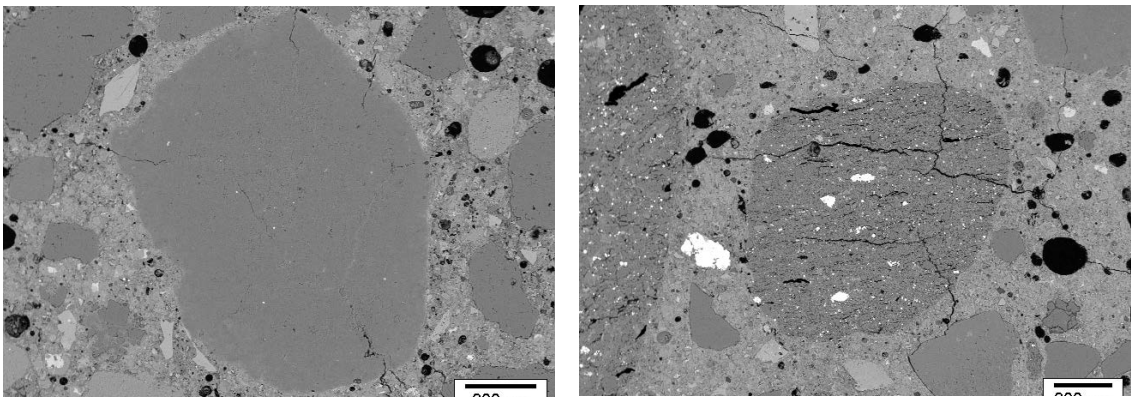

Figure A-58. SEM image of reacted chert (left) and siltstone (right) in H1.

Depth of Carbonation

Polished billets from the top surface of the cores were tested for depth of carbonation using the phenolphthalein method. Surprisingly, the recorded depths were relatively small (1 to 3mm) despite the high level of deterioration of the barriers.

Conclusion

According to this study, the primary cause of deterioration of the bridge barriers on the west bound of I94 over Middlebelt (bridge S06-82022) is ASR. Indeed, several fine siliceous fine aggregates showed signs of ASR: reaction rims, cracks extending through the paste, and presence of alkali-silica gel. Some fine siltstones were very likely also undergoing ASR (although in that case gel deposits were less apparent), and were possibly frost susceptible. The air-void system was found to be marginal in one of the cores, so freeze-thaw attack may exacerbate the deterioration. However, the latter is probably a consequence of the first deterioration mechanism (ASR), which favored the dissolution and precipitation of secondary deposits, compromising the initial air-void system. The major form of deterioration recorded on site was map cracking (68 percent of the surface was covered), which coincides well with the results since map cracking is a common manifestation of ASR.